ORIGINAL PAPER

Tin chloride perovskite-sensitized core/shell photoanode solar cell with spiro-MeOTAD hole transport material for enhanced solar light harvesting

P. Ananthajothi[1] · P. Venkatachalam[2]

Abstract An attempt has been made to fabricate methyl ammonium tin chloride ($CH_3NH_3SnCl_3$) perovskite-sensitized TiO_2 nanostructure photoanode solar cell with hole transport material (HTM) spiro-MeOTAD and graphite-coated counter electrode (CE). The TiO_2 nanoparticles (TNPs), TiO_2 nanoleaves (TNLs), and TNLs with MgO core/shell photoanodes were prepared to fabricate perovskite-sensitized solar cells (PSSCs). The prepared samples were characterized by X-ray diffraction (XRD), scanning electron microscopy (SEM), and transmission electron microscopy (TEM). The photovoltaic characteristics of the PSSCs, photocurrent density (J_{sc}), open-circuit voltage (V_{oc}), fill factor (FF), and power conversion efficiency (PCE) were determined under illumination of AM 1.5 G. Electrochemical impedance spectroscopy (EIS) analysis was carried out to study the charge transport and lifetime of charge carriers at the photoanode–sensitizer–electrolyte interface of the PSSCs. The PSSC made with $CH_3NH_3SnCl_3$ perovskite-sensitized TNL–MgO core/shell photoanode and spiro-MeOTAD HTM shows an impressive photovoltaic performance, with J_{sc} = 17.24 mA/cm^2, V_{oc} = 800 mV, FF = 73 %, and PCE = 9.98 % under 100 mW/cm^2 light intensity. The advent of such simple solution-processed mesoscopic heterojunction solar cells paves the way to realize low-cost and high-efficiency solar cells. By the aid of electrochemical impedance spectroscopy, it is revealed that the core/shell structure can increase an interfacial resistance of the photoanode–$CH_3NH_3SnCl_3$ interface and retard an electron recombination process in the photoanode–sensitizer–HTM interface.

Introduction

Perovskite solar cells based on organometallic halides represent an emerging photovoltaic technology. A highly efficient solar cell material should absorb light over a wide spectral range, generate charges with high efficiency, and transport these photogenerated charges to the electrodes with minimum losses. Several groups have reported power conversion efficiencies from 10 to 15 % for solution-processed organometallic halide perovskite-based solar cells in the past 2 years [1–3]. An organometallic perovskite with balanced long-range carrier diffusion lengths [4–6] and low cost has attracted great attention as a new class of light harvesters for solid-state hybrid solar cells in recent years [7]. Perovskites are unique as an active layer in photovoltaic (PV) modules, owing to their ability to deliver high open-circuit voltages, under full sun illumination, leading to light harvesting from a broad spectrum of incident solar radiation. In particular, the recent emergence of organic–inorganic halide perovskite-based solar cells promises to deliver one of the lowest-cost technologies that is capable of converting sunlight to electricity at the highest efficiencies [1, 8–10]. Good progress has been made in revealing the hybrid metallic halide perovskite to deliver impressive power conversion efficiency in solar cells. Synthetic perovskites have been identified as possible inexpensive base materials for high-efficiency commercial photovoltaic [11], and they showed a conversion efficiency of up to 15 % [3]. A

✉ P. Venkatachalam
pvchalamphyamu@gmail.com

1 Department of Physics, Annamalai University, Annamalai Nagar, Tamil Nadu 608002, India

2 Department of Physics, DDE, Annamalai University, Annamalai Nagar, Tamil Nadu 608002, India

group of methyl ammonium tin and lead halides is of interest for use in solar cells [12]. Among organic–inorganic perovskite-structured semiconductors, the most common one is the triiodide (CH$_3$NH$_3$PbI$_3$). It exhibits high-charge carrier mobility and carrier lifetime that allow light-generated electrons and holes to move far enough to be extracted as current, instead of losing their energy as heat within the cell. As we know, lead poisoning is a type of metal poisoning [13]; hence, it should be replaced by Sn.

In thin photovoltaic film, optical management is an important key for harvesting light while ensuring higher efficiency. Organic sensitizers often limit light-harvesting ability because of their low absorption coefficients and narrow absorption bands. Recently, a new class of hybrid organic halide perovskite was introduced as a light-sensitizing material, showing strong absorption in a broad region of the visible spectrum (direct energy gap down to ~1.55 eV), good electron and hole conductivity, and high open-circuit voltages in photovoltaic devices [14]. Meanwhile, solid-state dye-sensitized solar cell (DSSC) was introduced in 1998 [15] and the liquid electrolyte was replaced by organic/inorganic hole transport materials. The drawback of the perovskite-sensitized liquid-type DSSC was the instability of the deposited CH$_3$NH$_3$PbI$_3$ in liquid electrolyte. Surface protection of the deposited CH$_3$NH$_3$PbI$_3$ is thus to be developed to increase its stability in liquid-based DSSCs. The instability issue was actually solved by replacing liquid electrolyte with solid hole conductor spiro-MeOTAD, where an efficiency as high as 9.7 % was achieved from a very thin TiO$_2$ film (~0.5 μm) together with excellent long-term stability [16]. Perovskites are hybrid-layered materials typically with an AMX$_3$ structure, with A being a large cation, M a smaller metal cation, and X an anion from the halide series [17–19]. The perovskite-sensitized solar cell (PSSC) device structure and the octahedral structure of perovskite are shown in Fig. 1a, b, respectively.

Metallic oxide nanostructures have also been integrated into DSSCs to maximize the number of adsorbed dyes and thereby maximize the photocurrent. Titanium dioxide (TiO$_2$) has several advantages such as chemical stability, non-toxicity, good electrical property, and inexpensive material; therefore, it is extensively used in many applications such as photocatalyst, hydrogen production, and solar cells [20–23]. Anatase, rutile, and brookite are three main crystalline structures of titanium dioxide [22]. Anatase TiO$_2$ has bandgap energy of 3.2 eV of which the absorption thresholds correspond to 380 nm, suggesting that photoelectron transfer is easy under solar light irradiation. To avoid recombination of charge carriers, the core/shell structure, which acts as the energy barrier for physical separation of injected electrons from hole transport material (HTM), was used. It reduced the dark current and increased the open-circuit voltage. Accordingly, the enhanced photocurrent and open-circuit voltage have led to a prominent increase in photovoltaic efficiency. MgO has distinctive properties: high refractive index, wide optical bandgap, and low absorption and dispersion in visible and near-infrared spectral regions [24]. In the present investigation, an attempt has been made to study the performance of PSSCs fabricated based on various photoanode structures applied with a CH$_3$NH$_3$SnCl$_3$ perovskite sensitizer and spiro-MeOTAD electrolyte. The PSSCs are subjected to J–V characteristics for their power conversion efficiency (PCE) and other solar cell parameters. The electron impedance parameters at the photoanode–sensitizer–electrolyte interface were investigated by electrochemical impedance spectroscopy.

Experimental

All chemicals used in this study were of high purity which were purchased from Sigma-Aldrich, India, and were used without further purification unless otherwise stated. Bulk TiO$_2$, TiO$_2$ nanoparticles (TNPs), and TiO$_2$ nanoleaves (TNLs) paste were coated uniformly onto a fluorine-doped tin oxide (FTO) glass plate by the doctor blade technique with a thickness of ~10 μm.

Preparation of TNPs and TNLs through sol–gel process

TNPs were synthesized using titanium(IV) isopropoxide (TTIP), nitric acid, ethyl alcohol, and distilled water through a sol–gel process. Seventy milliliters of TTIP was mixed with 100 ml of ethanol, and 50 ml of distilled water was added drop by drop under vigorous stirring for 1 h. This solution was then peptized using 0.1 M of nitric acid (430 ml) and heated under reflux at 80 °C for 8 h. After this period, a TiO$_2$ sol was prepared. The prepared sol was dried to yield a TiO$_2$ powder.

Fig. 1 a Schematic diagram of PSSC. b Crystal structure of the orthorhombic CH$_3$NH$_3$SnX$_3$ (X = Cl) perovskite
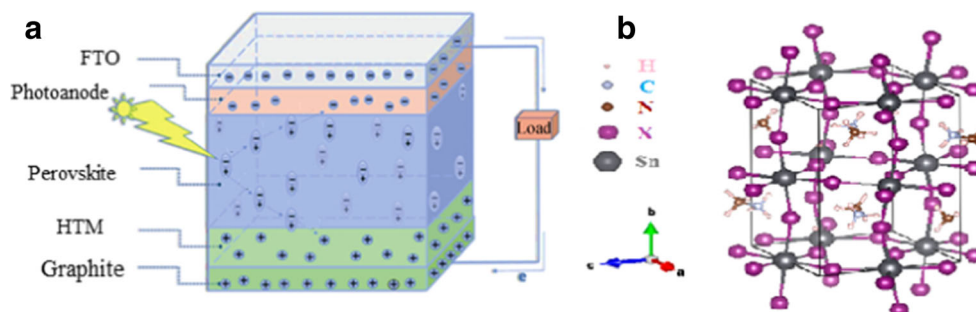
The TiO$_2$ was calcined at 450 °C for 1 h in a furnace to get TNPs. TNLs were prepared through an alkali hydrothermal process. Two grams of TNPs prepared from the sol–gel method was mixed with 100 ml of a 10 M NaOH aqueous solution, followed by hydrothermal treatment at 150 °C in a Teflon-lined autoclave for 12 h. After the hydrothermal reaction, the treated sample was washed thoroughly with distilled water and 0.1 M HCl and subsequently filtered and dried at 80 °C for 1 day. To achieve the desired TNL size and crystallinity, the sample was calcined at 600 °C for 1 h [25].

Preparation of the MgO shell coating

In a typical process, the MgO shell coating was prepared by dipping the TNL electrode into a saturated magnesium methoxide solution and then washing thoroughly with distilled water. After drying, the electrode was calcined at 450 °C for 0.5 h. The thickness of the shell layer (~5 nm) was controlled by the dipping time [26].

Synthesis of metallic halide CH$_3$NH$_3$SnCl$_3$ perovskite sensitizer

CH$_3$NH$_3$Cl was synthesized by reacting 30 ml of methylamine (40 % in methanol) and 32.3 ml of hydrochloric acid (57 wt% in water) in a 250-ml round-bottom flask at 0 °C for 2 h with stirring. The precipitate was recovered by putting the solution on a rotary evaporator and carefully removing the solvents at 50 °C. The yellowish raw product methyl ammonium chloride (CH$_3$NH$_3$Cl) was washed with diethyl ether by stirring the solution for 30 min, a step which was repeated three times, and then finally recrystallized from a mixed solvent of diethyl ether and ethanol. To prepare CH$_3$NH$_3$SnCl$_3$, the readily synthesized CH$_3$NH$_3$Cl (0.395 g) and SnCl$_2$ (1.157 g) were mixed in 10 ml of dimethylformamide (DMF) at 60 °C for overnight with stirring. The small beaker is immediately sealed and kept in the dark at room temperature [27]. Aluminum foil is used over the lid of the sample beaker to prevent reaction with sunlight.

Fabrication of perovskite-sensitized solar cells

The photoanodes using bulk TiO$_2$, TNPs, TNLs, and TNL–MgO core/shell were prepared by ultrasonically mixing for 2 h. The prepared pastes were deposited by the doctor blade technique on FTO (8–10 Ω/sq) by preparing an active area of 1 cm^2. Four types of photoanodes (bulk TiO$_2$, TNPs, TNLs, and TNL–MgO core/shell) were respectively labeled as PSSC-1, PSSC-2, PSSC-3, and PSSC-4. The film was then heated to 450 °C at a rate of 15 °C/min and kept at 450 °C for 30 min. The perovskite precursors were then spin-coated on the TiO$_2$-coated FTO substrate at a speed of 3000 rpm for 30 s, followed by immediate annealing on a hot plate at various temperatures

for different time spans. The color of the samples finally turned into dark brown, indicating the formation of the perovskite phase. The annealing temperature would lead to the change of the perovskite morphology and formation of larger crystalline particles on the surface of mesoporous TiO$_2$ film substrate. The smooth morphology of perovskite film was achieved through adjusting the concentrations of mixed DMF solution [28]. After cooling down to room temperature, the hole transport material layer was deposited onto the perovskite layer with a thickness of 100 nm by spin coating 50 μL of the spiro-MeOTAD solution at a speed of 4500 rpm for 40 s. The hole transport material contains 0.170 M 2,2′,7,7′-tetrakis(*N,N*-dipmethoxyphenylamine)-9,9′-spirobifluorene (spiro-MeOTAD, Merck), 0.064 M bis(trifluoromethane)sulfonimide lithium salt (LiTFSI, 99.95 %, Sigma-Aldrich), and 0.198 M 4-*tert*-butylpyridine (TBP, 96 %, Sigma-Aldrich) in the mixed solvent of chlorobenzene (99.8 %, Sigma-Aldrich) and acetonitrile (99.8 %, Sigma-Aldrich) (chlorobenzene:acetonitrile 51:0.1 *v/v*). A graphite-coated counter electrode (CE) was then clipped on top of the photoelectrode to form a photovoltaic device.

Characterization of PSSCs

The photovoltaic properties of the PSSCs were characterized by recording the photocurrent voltage (*J–V*) under illumination of AM 1.5 G (100 mW/cm^2). The prepared photoanode using bulk TiO$_2$, TNPs, TNLs, and TNL–MgO core/shell structures was characterized by X-ray diffraction (XRD) (X'Pert PRO-PANalytical X-ray powder diffractometer). Transmission electron microscopy (TEM) characterization was done by a Philips Tecnai 10 electron microscope operated at 200 kV. Scanning electron microscopy (SEM) images were recorded by a VEGA3 SB electron microscope. Specific surface areas of the TiO$_2$ samples are determined by the use of a nitrogen adsorption apparatus (Micromeritics ASAP 2020). Electrochemical characteristics of the PSSCs were recorded with a potentiostat/galvanostat (Gamry 300). The applied bias voltage and ac amplitude were set at open-circuit voltage of the PSSCs and 10 mV between the FTO/counter electrode and the FTO/photoanode, respectively, and the frequency range explored was 1 MHz to 10^5 Hz. The impedance spectra were analyzed by an equivalent circuit model interpreting the characteristics of the PSSCs.

Results and discussion

XRD, TEM, and SEM analysis

The crystalline structure of the bulk TiO$_2$, TNPs, TNLs, and TNL–MgO core/shell was characterized by XRD and is given in Fig. 2. The XRD pattern of TNL–MgO consists of anatase TiO$_2$ and MgO peaks. The peaks observed at 25.3°, 37.9°, 48.0°, 53.9°, and 62.6° correspond to the planes (101), (004),
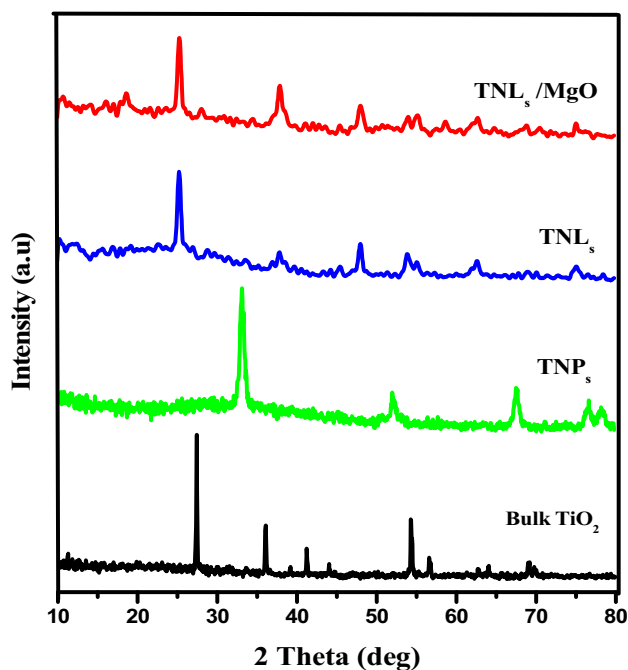
Fig. 2 XRD patterns of the TiO$_2$ samples

(200), (105), and (215) of anatase phase (JCPDS 21-1272) [29]. The observed peaks are very sharp, implying that the TNLs were well crystallized and additional peaks observed in this diffractogram might be due to the calcinations of the sample during a hydrothermal process. The peaks appeared at 43.2° and 62.3° correspond to the (200) and (220) planes of the MgO phase, respectively [26]. The narrow peaks observed in the XRD pattern of bulk TiO$_2$ illustrated the bigger particle size of the sample. However, the XRD pattern of the TNP exemplifies broadening of peaks at 33.5°, 54.2°, and 68.6°. The periodicity of the individual crystallite domains reinforces the diffraction of the X-ray beam, resulting in a tall narrow peak. If the crystals are randomly arranged or have low degrees of periodicity, the result is a broader peak. This is normally the case for nanomaterial assemblies [30]. Figure 3a, b shows the TEM image of TNPs and TNL–MgO core/shell, respectively.

Figure 3a depicts that the average diameters of the TNPs are 20–60 nm. From the Fig. 3b, it could be seen that the average diameter of the TNL–MgO core/shell is 5–10 nm. Figure 3c shows that the SEM image of the TNLs has a leaf-like structure. TNLs are very uniform, quite clean, and smooth-surfaced. It could be seen that the starting material exhibited the nanoparticles and, after hydrothermal synthesis, the nanoparticles were completely converted to TNLs. The textures of the TNLs are uniform and reasonably dense, though there are ample voids between the leaves. The Brunauer-Emmett-Teller (BET) surface area measurement revealed that the TNL–MgO core/shell had a specific area of 16 m^2/g. This value is much higher than that of TNPs (12 m^2/g) and TNLs (14 m^2/g).

Photovoltaic characterization

The photocurrent–voltage (J–V) characteristics of the PSSCs with various types of photoanodes are shown in Fig. 4. The detailed photovoltaic parameters such as open-circuit voltage (V_{oc}), short-circuit photocurrent density (J_{sc}), fill factor (FF), and PCE (η) of the PSSCs are presented in Table 1. The overall PCE of PSSCs is varied in the four types of TiO$_2$ photoanodes. The PSSC-4 showed the highest efficiency as compared to the other PSSCs. Photovoltaic parameters for the PSSC-4 are V_{oc} = 800 mV, J_{sc} = 17.24 mA, FF = 73 %, and η = 9.98 %. The PSSC-1 that is made with only bulk particle of TiO$_2$ showed the lowest photovoltaic parameters as follows: V_{oc} = 750 mV, J_{sc} = 6.47 mA, FF = 66 %, and η = 3.20 %. Photovoltaic parameters for the PSSC-2 prepared with the TNP photoanode are V_{oc} = 780 mV, J_{sc} = 9.65 mA, FF = 68 %, and η = 4.92 %. The PSSC-3 that is made using the TNL photoanode exhibited the photovoltaic parameters as follows: V_{oc} = 780 mV, J_{sc} = 14.16 mA, FF = 70 %, and η = 7.73 %. The efficiencies of the PSSCs were fabricated with different types of photoanode in the order of PSSC-4 > PSSC-3 > PSSC-2 > PSSC-1. These results suggested that the PSSC-4 fabricated through the TNL–MgO core/shell structure
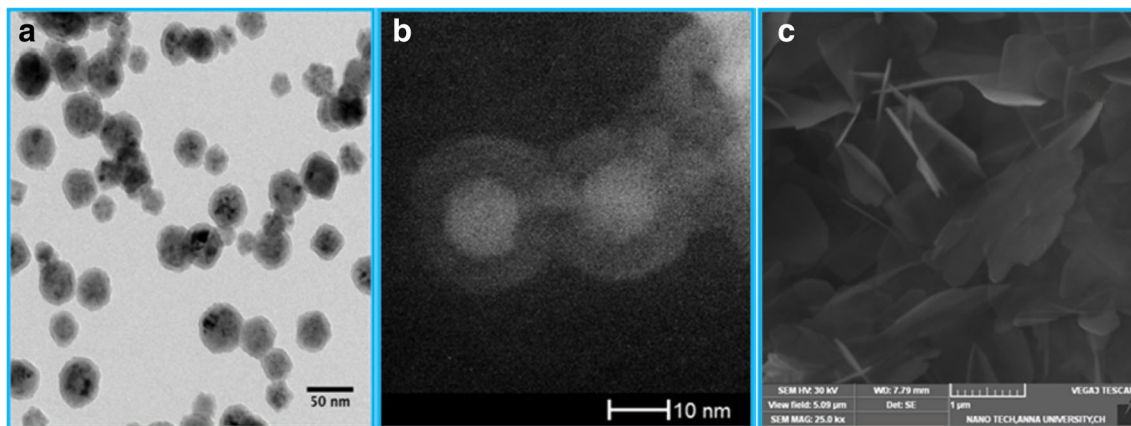

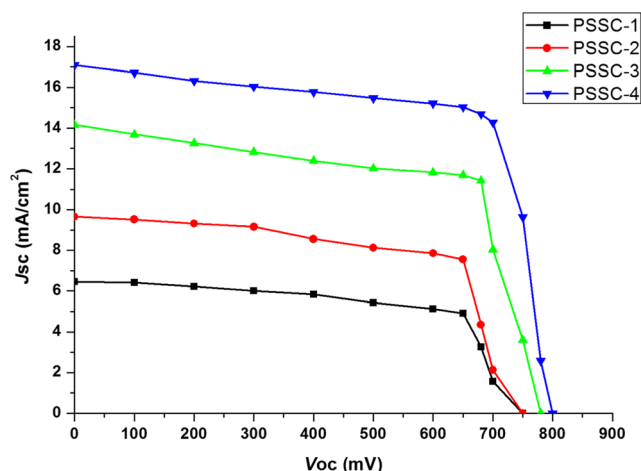**Fig. 3** .TEM images of TNPs (**a**) and TNL–MgO core/shell (**b**) and SEM image of TNLs (**c**)

Fig. 4 *J–V* characteristics of the PSSCs

holds more efficiency as compared to the other PSSCs. When comparing PSSC-4 and PSSC-3, the PSSC-4 showed enhanced efficiency due to the core/shell structure of TNL–MgO photoanode. By enclosure of MgO into the TNL film, the photovoltaic characteristics have been changed dramatically. As a result of the good photovoltaic parameters for the cell consisting of TNL–MgO core/shell photoanode, the highest η of 9.98 % is obtained at an optimized condition. The overall conversion efficiency was increased by 211 % from 3.20 to 9.98 % when comparing PSSC-1 and PSSC-4. The improvement of the efficiency was ascribed to the increase in the short-circuit current density (J_{sc}), V_{oc}, and FF. These results suggested that the electron injection is efficient through the MgO shell coating compared with the uncoated PSSC-3. A typical wide bandgap oxide, MgO, was often employed to form a core–shell-structured TiO$_2$ photoanode. The MgO shell can retard the recombination of injected electrons in the semiconductor and holes in the hole transporting material (HTM). The core–shell electrodes provide an inherent energy barrier at the photoanode–HTM interface, the electron recombination losses are remarkably reduced, and consequently, the V_{oc} values increase [31, 32]. The PSSC-1 has the lowest photocurrent efficiency because it was made up with the bulk TiO$_2$ photoanode without a core–shell structure.

Remarkably, the mesoporous *n*-type TiO$_2$ with insulating MgO, CH$_3$NH$_3$SnCl$_3$ sensitizer, and spiro-MeOTAD HTM electrolyte improved the power conversion efficiency to 9.98 %. Perovskites as an active layer are unique in photovoltaic

Table 1 PCE of the PSSCs using various electrodes

PSSCs	V_{oc} (mV)	J_{sc} (mA/cm^2)	FF (%)	η (%)
PSSC-1	750	6.47	66	3.20
PSSC-2	750	9.65	68	4.92
PSSC-3	780	14.16	70	7.73
PSSC-4	800	17.24	73	9.98

modules, owing to their ability to deliver high open-circuit voltages, under full sun illumination, leading to light harvesting from a broad spectrum of incident solar radiation [33]. In the present investigation, the PSSC-4 has exhibited higher V_{oc} of 800 mV. HTMs are solid-state mediators which are absolutely free from leakage. In dye-sensitized solar cells with HTMs, hole transfer takes place directly from the sensitizer to the HTM and the holes are transported via electron hopping to a metal counter electrode. Here, we used HTM, spiro-MeOTAD which has small molecular size, high solubility, and amorphous nature, and thus solid-state PSSC-4 attained the PCE of 9.98 %.

Electrochemical impedance spectroscopy analysis

Electron transport properties were investigated using electrochemical impedance spectroscopy. Figures 5 and 6 show the Nyquist and frequency-phase plots of PSSCs, respectively. In order to understand the electrical behavior and observe how the device parameters change with any kind of applied treatment (bias, illumination, etc.) to the device, it is modeled with discreet electrical components such as voltage or current sources, diodes, and resistors. It provides a scientific and realistic physical explanation for the PV behavior. The ac response of the cell is conventionally described by an equivalent circuit. At each frequency, the equivalent circuit provides a full representation of the electric potential distribution in the system. While the circuit model is largely dependent on system specifics, the usual configuration of elements is that represented in Fig. 7. Figure 5 illustrates the Nyquist plots corresponding to the PSSCs based on the metallic halide perovskite-sensitized photoanode film under the light intensity of 100 mW/cm^2. Generally, all the Nyquist plots of PSSCs exhibit three semicircles, which are assigned to electrochemical reaction at the graphite counter electrode, charge transfer at the photoanode/perovskite/HTMs, and Warburg diffusion process. The equivalent circuit consists of a series of resistance (R_s, starting point
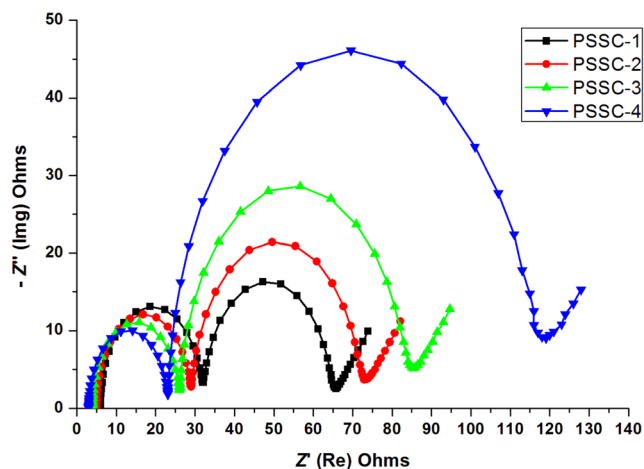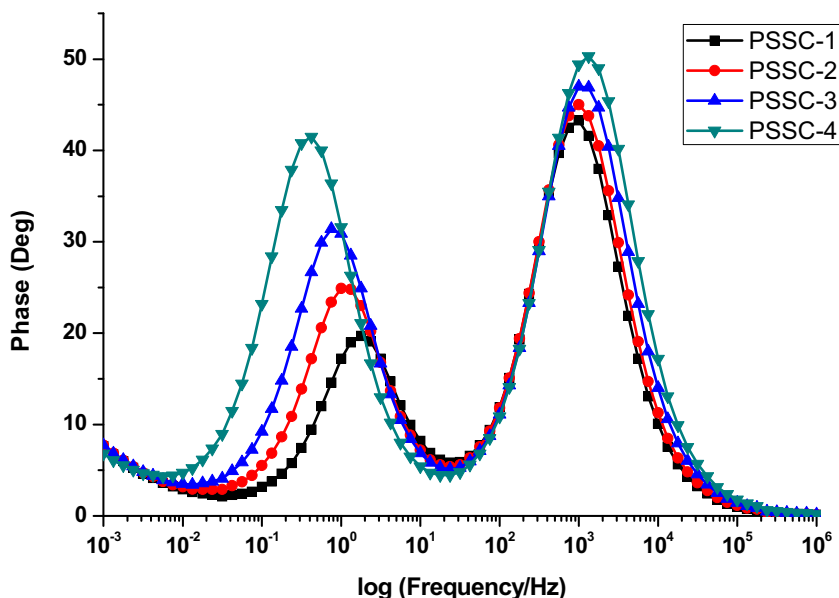

Fig. 5 Nyquist plot of electrochemical impedance spectroscopy (EIS) of the PSSCs

Fig. 6 Phase versus frequency plot of the PSSCs

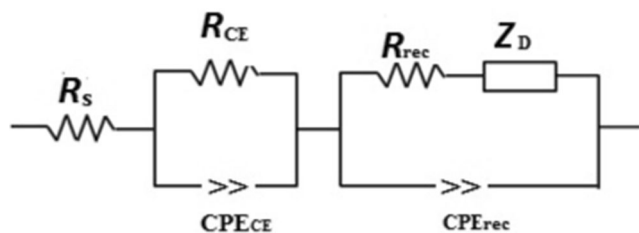of the first semicircle in the Nyquist plot), electron transport resistance at the counter electrode/electrolyte (R_{CE}, first semicircle in the Nyquist plot), recombination resistance (R_{rec}) at the photoanode/perovskite/HTM (second semicircle in the Nyquist plot), the constant phase elements of capacitance CPE_{rec} (R_{rec}) and CPE_{CE} (R_{CE}), and Warburg diffusion impedance (Z_d) which are shown in Fig. 7. The other useful electrochemical parameters of PSSCs are τ_n (electron lifetime, Eq. (1)), L_n (electron diffusion length, Eq. (2)), D_{eff} (effective diffusion coefficient, Eq. (3)), μ (electron mobility, Eq. (4)), σ (electron conductivity, Eq. (5)), η_{cc} (electron collection efficiency, Eq. (6)), and Conc. (concentration of electrons in the TiO$_2$–sensitizer–HTM interface, Eq. (7)) and are calculated in the following equations [26] and presented in Table 2:

$$\tau_n(s) = R_{rec} \, CPE_{rec} \tag{1}$$

$$L_n(ms) = L_F \sqrt{\frac{R_{rec}}{R_{tr}}} \tag{2}$$

$$D_{eff}\left(cm^2/s\right) = \frac{L_n^2}{\tau_n} \tag{3}$$

$$\mu\left(\frac{cm^2}{V/s}\right) = \frac{(D_{eff}\,e)}{K_B T} = 38.9 D_{eff} \tag{4}$$

$$\sigma\left(s/cm\right) = \frac{L_F}{[S(1-P)R_{tr}]} \tag{5}$$

$$\eta_{cc} = 1 - \left(\frac{\tau_d}{\tau_n}\right) \tag{6}$$

$$Conc.\left(\Omega \; cm/s\right) = R_{rec} \; L_F \; k_{eff} \tag{7}$$

where L_F is the film thickness of the photoanode (10 μm), S is the active area of the PSSCs (1 cm^2), P is the porosity of the photoanode film (0.6), τ_d is the electron transport time (R_{tr} CPE_{rec}), e is the charge of an electron, K_B is the Boltzmann constant, T is the room temperature, and k_{eff} is the rate of recombination of the electrons $\left(\frac{1}{\tau_n(s)}\right)$.

From the Nyquist plots, it could be seen that the first and third semicircles are weak when compared with the second semicircle. In this study, HTM offers low diffusive resistance and better mobility of holes; thus, we got a straight line observed in the low-frequency region. The low-frequency loop is characterized by part at 45°, which suggests limiting steps due to charge carrier diffusion. The question of its origin remains open and has not been clearly established for TiO$_2$-based PSSCs in the recent literature [34, 35]. From Fig. 5 comparing the middle semicircles of the Nyquist plot of the PSSCs, the R_{rec} value increases in the order of PSSC-1 < PSSC-2 < PSSC-3 < PSSC-4 which indicates that the larger the value of R_{rec}, the lower the recombination rate at the photoanode–sensitizer–HTM interface. The PSSC-4 fabricated with the TNL–MgO core/shell photoanode illustrated higher values of CPE_{rec}, L_n, τ_n, D_{eff}, μ, σ, and η_{cc} at the photoanode–sensitizer–HTM interface as compared with other PSSCs. In addition, R_{tr} and concentration of electrons at the photoanode–sensitizer–HTM interface have lower values as compared with the

Fig. 7 EIS equivalent circuit diagram

Table 2 EIS parameters obtained from the Nyquist plots of PSSCs

| PSSCs	R_{tr} (Ω)	R_{rec} (Ω)	CPE_{rec} (10^{-3})	τ_n (ms)	L_n (μm)	D_{eff} (10^{-6}; cm^2/s)	μ (10^{-5}; cm^2/V/s)	σ (10^{-5}; S/cm)	Conc. (Ω cm/s)	η_{cc} (%)
PSSC-1	20	32	3.98	127.36	1265	12.56	48.87	8.33	0.251	37
PSSC-2	14	42	5.25	220.50	1732	13.61	52.93	14.29	0.190	66
PSSC-3	11	56	6.26	350.56	2256	14.52	56.49	22.72	0.159	80
PSSC-4	5	90	9.86	887.40	4243	20.28	78.90	66.67	0.101	94

other PSSCs. These results enabled not only the reduction of the recombination rate but also the enhancement of the η_{cc} in PSSC-4. Control of interfacial electron injection and recombination in the photoanode–sensitizer–HTM interface is pivotal for the best performance of PSSCs. This implied that the recombination rate was diminished because the doped MgO could shield the electron backflow through the TNLs to the electrolyte. Thus, the surface modification of the photoanode with very thin layer as well as larger bandgap shell material improved the photocurrent density. Hence, the core–shell material provided faster electron injection and suppressed recombination at the photoanode–sensitizer–HTM interface. In our examination on the performance of core–shell structure-based PSSCs, hints that the essential improvement in electron injection efficiency and thereby overall performance can be obtained by proper designing of the second metallic oxide with suitable bandgap, optimal thickness of shell layer, and isoelectric point. In addition to the TNL structure, the grain boundaries effect could be restricted [36, 37]. Moreover, for the same given film thickness, the loading of dye can be much higher in the TNLs than in the TNPs; for instance, the TNLs have allowed for larger adsorption of the sensitizer. This necessitates the development of new nanostructures for electron separation and conduction such as TiO$_2$ nanorods [38, 39] and nanosheets [27] with the objective of improving electron transport and absorber infiltration as well as exploration of novel HTMs with suitable band alignment and improved hole mobilities [2]. The enhanced efficiencies of the TNL–MgO core–shell PSSCs are achieved by optimizing device architectures, which enhanced light absorption and facilitated electron transport by determining and designing appropriate dimensions of TNL–MgO, by optimizing the cation concentration in the HTM for promoting electron injection yield from sensitizing CH$_3$NH$_3$SnCl$_3$ molecules to core–shell TNL–MgO electrodes, or by synthesizing thermally stable TNLs with a stable high surface area. In the core–shell TNL–MgO photoanode, the higher R_{rec} suggested that each TNL made it more difficult for an electron to jump outside the nanostructure than to stay within the structure during diffusion; this explained the high collection efficiency and thus high short-circuit photocurrent.

Figure 6 shows the frequency-phase plots of EIS spectra for the PSSCs, made with different photoanodes. Two characteristic peaks associated with the transfer of the photo-generated electrons at the surface of TNL–MgO core/shell and the conducting electrodes are clearly observed. The frequency peak at the high-frequency region can be ascribed to the charge transfer at the interfaces of the electrolyte/counter electrode and the other low-frequency regions to the accumulation/transport of the injected electrons with TNL–MgO core/shell porous film and the charge transfer at the interfaces of electrolyte, respectively. From Fig. 6 which shows the frequency-phase plots in the lower-frequency regime, it can be seen that the frequency peak of PSSC-1 shifted to lower frequency when compared with that of PSSC-3 and PSSC-4. The characteristic frequency peak of PSSC-4 in higher-frequency regime shifted to the higher-frequency region when compared to other PSSCs. This result could be attributed to the higher electron transport rate and electron diffusion coefficient of PSSC-4. The increase of the electron lifetime makes the electron diffusion and transfer more easily due to the increase of the diffusion length [40]. These results indicate that TNL–MgO core/shell photoanode PSSCs have higher electron transport and lower recombination rate at the photoanode–sensitizer–HTM interface and the same property leading to higher solar cell efficiency. In the present investigation, 9.98 % efficiency is remarkable, considering the HTM electrolyte and graphite-coated counter electrode employed.

In these devices, the electrons are transported through the perovskite layer and the holes are transported through the
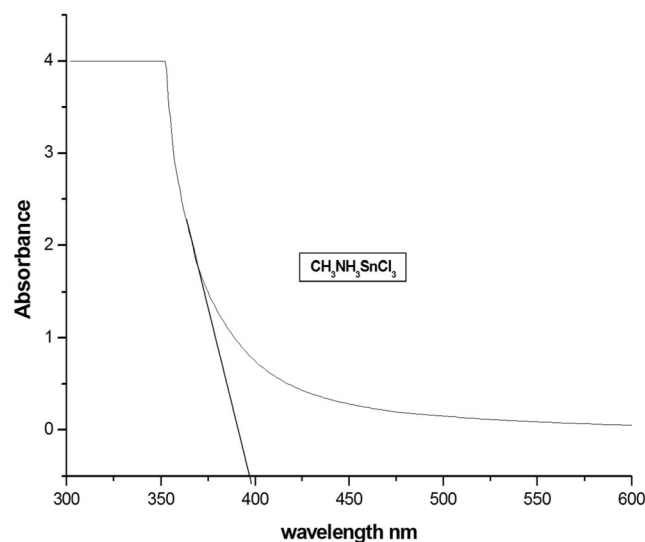
**Fig. 8** UV-visible spectra of CH$_3$NH$_3$SnCl$_3$
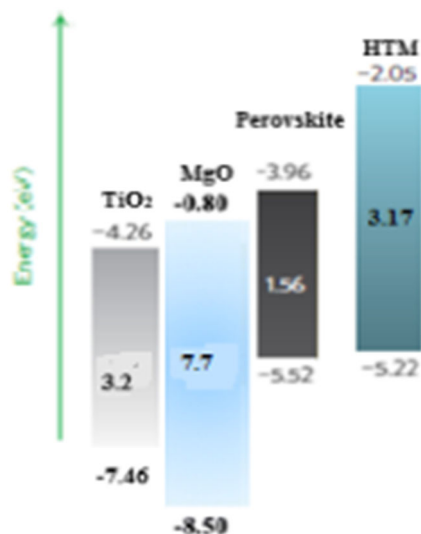
Fig. 9 Energy level diagram of the PSSC

spiro-MeOTAD layer. It is interesting to note that the perovskite layer can function as a light absorber as well as *n*-type semiconductor for transporting electronic charges out of the device. In the perovskite sensitizer, the inorganic component is an ionic crystal and then native dipoles would occur at the organic–inorganic interface, between the hole transporter and the perovskite. Indeed, the presence of under-coordinated halide at the crystal surface gives rise to local excess of negative electrostatic charge, which may trap the holes injected into the spiro-MeOTAD, generating interfacial dipoles. Recombination of electrons in TiO$_2$ with holes in the perovskite itself is moreover unlikely to be very fast, since the hole density in the perovskite should be relatively low due to their high diffusivity and effective transfer to spiro-MeOTAD at the planar heterojunction [5]. The same applies for the recombination of holes in spiro-MeOTAD with electrons in the perovskite: the electron density in the perovskite will be very low due to the fast electron transfer to the TiO$_2$ nanoparticles, meaning this recombination mechanism will also be very slow. The understanding gained here allows us to propose design rules for

preparing high-efficiency TiO$_2$-based perovskite solar cells. The most important factor to control is the completeness of perovskite coverage on the TiO$_2$ nanoparticles, as this reduces recombination rates. This means that higher charge densities can be maintained in the TiO$_2$, improving the charge transport rates and collection efficiencies of the solar cells. This, together with the fact that thinner TiO$_2$ scaffolds serve to concentrate the electron density at a given generation rate, also leads to an increase of the electron quasi Fermi level in the TiO$_2$ to improve the photovoltage of the solar cells.

A good photovoltaic absorber needs to have strong absorption over a wide range of spectrum to minimize the amount of material usage and reduce charge and energy loss during extraction to electrodes. One superior property of the perovskite materials to this end is its very high absorption coefficient with the sharp onset of absorption edge. Material computation showed that the perovskite materials are direct bandgap semiconductor materials [41]. The absorption coefficient is calculated as 4.2×10^4 in the visible range, which indicates that the perovskite material only needs 395 nm to absorb 90 % of the visible light by taking into consideration the electrode reflection [42]. As a matter of fact, most of the reported high-efficiency devices had a thickness around 300–600 nm [43]. In the present investigation, the thickness of the perovskite layer is measured as 300 nm. The absorption edge of the perovskite film shows a very sharp onset which indicates the absence of deep states shown in Fig. 8. Our findings show that the perovskite-sensitized solar cell PSSC-4 had highly mobile electron, the holes are formed within a few picoseconds, and the mobilities of both are almost balanced and remain high. Low recombination and almost equal electron and hole mobilities guarantee a very efficient charge collection and thus high solar cell efficiency. The results also show that, as a consequence of electron injection from the perovskite to the core/shell photoanode with very high electron mobility, the overall mobility is higher. The energy level diagram of PSSC is shown in Fig. 9. A possible improvement of solar cell performance would be the active materials such that both

Fig. 10 Stability of the PSSCs
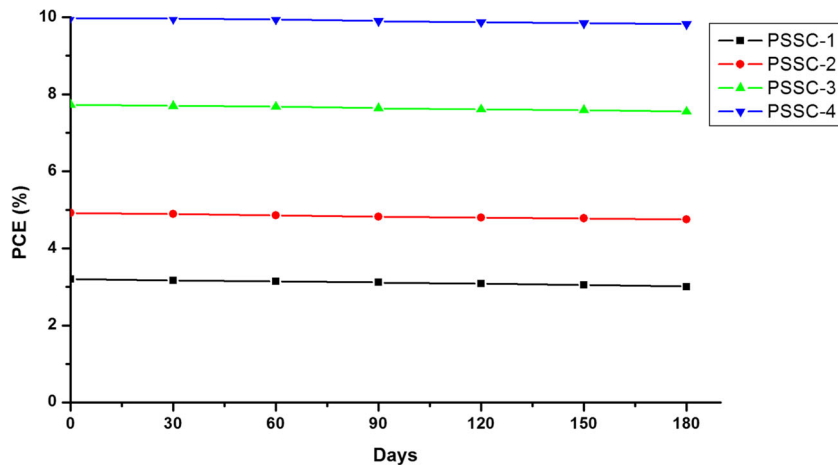
electron and hole mobilities are on the level of the electron mobility in the perovskite. Despite the disadvantage of platinum counter electrode/electrolyte in DSSC, higher cost, poor stability in corrosive electrolyte, and high-temperature processing drives, the need for the development of alternative CE materials. In the recent past, a few groups reported on different CE materials like carbon nanotubes (CNTs) [3, 27], activated carbon, and graphite [44]. In this study, graphite has been used as a counter electrode. It has also been reported that humidity degrades the $CH_3NH_3PbI_3$ performance. Halide alteration has been promising in this regard with increased stability in humid environments at minor performance penalty [45] occurring when a low proportion of Cl is introduced. Lead content is another drawback for the viability of these cells. Hence, in this investigation, PSSCs fabricated by incorporating the core–shell photoanode structure, $CH_3NH_3SnCl_3$ perovskite sensitizer, the HTM electrolyte, and graphite counter electrode offered better PCE performance. In this study, Pb was replaced by Sn; thus, stability is significantly increased as shown in Fig. 10. The device PSSC-4 illustrated the PCE of 9.82 % after 180 days.

Conclusions

TNPs and TNLs were synthesized via sol–gel and hydrothermal transformation, respectively. PSSCs made of different types of TiO_2-working photoanode were constructed. The electron transport resistance, electron lifetime, and diffusion length were evaluated in terms of electrochemical impedance spectra and photovoltaic characteristics of the cells. The PSSC-4 based on the core–shell structure of TNL–MgO photoanode hybrids showed a better photovoltaic performance (higher FF, open-circuit voltage, and photocurrent density) than the cell purely made of TNPs. The PSSC-4 showed the PCE conversion efficiency of 9.98 % which is higher than that of other PSSCs. From these results, it could be concluded that the TNL–MgO core–shell novel photoanode structure possibly could restrain the recombination process and increase the PCE effectively. The new core/shell with perovskite sensitizer architecture presented a large open spacing and mediator/electrolyte access. In addition, the PSSC made up of the spiro-MeOTAD electrolyte showed better performance and has relatively high ambient and ionic conductivity intimate interfacial contact with TNL–MgO core/shell and remarkable stability. The present work establishes that the cell with the $CH_3NH_3SnCl_3$-sensitized TNL–MgO core/shell photoanode heterojunction with the spiro-MeOTAD electrolyte had better performance. We conclude that the perovskite is stable in dry ambient air and can be deposited by low-cost solution processing that opens up new avenues for the future development of high-efficiency low-cost photovoltaic cells.

References

1. Lee MM, Teuscher J, Miyasaka T, Murakami TN, Snaith HJ (2012) Science 338:643–647
2. Heo JH, Im SH, Noh JH, Mandal TN, Lim CS, Chang JA, Lee YH, Kim H (2013) Nat Photonics 7:486–491
3. Burschka J, Pellet N, Moon SJ, Baker RH, Gao P, Nazeeruddin MK, Grätzel M (2013) Nature 499:316–319
4. Xing G, Mathews N, Sun S, Lim SS, Lam YM, Grätzel M, Mhaisalkar S, Sum TC (2013) Science 342:344–347
5. Stranks SD, Eperon GE, Grancini G, Menelaou C, Alcocer MJP, Leijtens T, Herz LM, Petrozza A, Snaith HJ (2013) Science 342:341–344
6. Edri E, Kirmayer S, Cahen D, Hodes G (2013) J Phys Chem Lett 4:897–902
7. Snaith HJ (2013) J Phys Chem Lett 4:3623–3630
8. Kojima A, Teshima K, Shirai Y, Miyasaka T (2009) J Am Chem Soc 131:6050–6051
9. Kim HS, Lee CR, Im JH, Lee KB, Moehl T, Marchioro A, Moon SJ, Baker RH, Yum JH, Moser JE (2012) Sci Rep 2:591–597
10. Kim HS, Im SH, Park NG (2014) J Phys Chem C 118:5615–5625
11. Bihui G, Gang L, Lijuan L, Yiwen T (2010) J Nat Sci 15:325–329
12. Angewadte BVL (2014) Chem Int Ed 53:635–637
13. Service R (2013) Science 342:794–797
14. Gidlow DA (2004) Occup Med 54:76–81
15. Mosconi E, Amat A, Nazeeruddin MK, Grätzel M, De Angelis F (2013) J Phys Chem C 117:13902–13913
16. Bach U, Lupo D, Comte P, Moser JE, Weissörtel F, Salbeck J, Spreitzer H, Grätzel M (1998) Nature 395:583–585
17. Arend H, Huber W, Mischgofsky FH, Richtervan Leeuwen GK (1978) J Cryst Growth 43:213–223
18. Umebayashi T, Asai K, Kondo T, Nakao A (2003) Phys Rev B 67:155405–115506
19. Baikie T, Fang Y, Kadro JM, Schreyer M, Wei F, Mhaisalkar SG, Graetzel M, White TJ (2013) J Mater Chem A 1:5628–5641
20. Eperon GE, Stranks SD, Menelaou C, Johnston MB, Herz LM, Snaith HJ (2014) Energy Environ Sci 7:982–988
21. Fujishima A, Rao TN, Tryk DA (2000) J Photochem Photobiol C 1:1–21
22. Pirkanniemi K, Sillanpää M (2002) Chemosphere 48:1047–1060
23. Hu Y, Tsai HL, Huang CL (2003) J Eur Ceram Soc 23:691–696
24. Li B, Lü G, Luo L, Tang Y (2010) Wuhan Univ J Nat Sci 15:325–329
25. Ananthajothi P, Venkatachalam P (2015) Int Res J Eng Technol 2:785–791
26. Maheswari D, Venkatachalam P (2015) J Electron Mater 44:967–976
27. Etgar L, Gao P, Xue Z, Peng Q, Chandiran AK, Liu B, Nazeeruddin MK, Grätzel M (2012) J Am Chem Soc 134:17396–17399
28. Shahbazi M, Wang H (2016) Sol Energy 123:74–87
29. He XYJ, Peng JF, Chu W, Lia YZ, Tong DG (2014) J Mater Chem A 2:1721–1731
30. Chen X, Mao SS (2007) Chem Rev 107:2891–2959
31. Zhang S, Yang X, Qin C, Numata Y, Han L (2014) J Mater Chem A 2:5167–5177

32. Avellaneda CO, Gonçalves AD, Benedetti JE, Nogueira AF (2010) Electrochim Acta 55:1468–1474
33. Snaith HJ (2010) Adv Funct Mater 20:13–19
34. Dualeh A, Moehl T, Tétreault N, Teuscher J, Gao P, Nazeeruddin MK, Grätzel M (2014) ACS Nano 8:362–374
35. Gonzalez-Pedro V, Juarez-Perez EJ, Arsyad WS, Barea EM, Fabregat-Santiago F, Mora-Sero I, Bisquert J (2014) Nano Lett 14:888–893
36. Fujihara K, Kumar A, Jose R, Ramakrishna S, Uchida S (2007) Nanotechnology 18:365709–365713
37. Baxter JB, Aydil JB (2006) Sol Energy Mater Sol Cells 90:607–622
38. Kim HS, Lee JW, Yantara N, Boix PP, Kulkarni SA, Mhaisalkar S, Gratzel M, Park NG (2013) Nano Lett 13:2412–2417
39. Qiu J, Qiu Y, Yan K, Zhong M, Mu C, Yan H, Yang S (2013) Nanoscale 5:3245–3248
40. Hamadanian M, Jabbari V, Gravand A, Asad M (2012) Surf Coat Technol 206:4531–4538
41. Yin WJ, Shi T, Yan Y (2014) Adv Mater 26:4653–4658
42. Green MA, Ho-Baillie A, Snaith HJ (2014) Nat Photonics 8:506–514
43. Xiao Z, Yuan Y, Wang Q, Shao Y, Yang B, Deng Y, Dong Q, Hu M, Cheng B, Huang J (2016) Mater Sci Eng R 101:1–38
44. Imoto K, Takahashi K, Yamaguchi T, Komura T, Nakamura JI, Murata K (2003) Sol Energy Mater Sol Cells 79:459–469
45. Noh JH, Im SH, Heo JH, Mandal TN, Seok SI (2013) Nano Lett 13:1764–1769